

# Projection effects in the strong lensing study of subhaloes

Ran Li,<sup>1,2\*</sup> Carlos S. Frenk,<sup>3</sup> Shaun Cole,<sup>3</sup> Qiao Wang<sup>1</sup> and Liang Gao<sup>1</sup>

<sup>1</sup>Key laboratory for Computational Astrophysics, National Astronomical Observatories, Chinese Academy of Sciences, Beijing 100012, China

<sup>2</sup>College of Astronomy and Space Sciences, University of Chinese Academy of Sciences, 19A Yuquan Road, Beijing 100049, China

<sup>3</sup>Department of Physics, Institute for Computational Cosmology, University of Durham, South Road, Durham DH1 3LE, UK

Accepted 2017 March 2. Received 2017 March 2; in original form 2016 August 15

## ABSTRACT

The defining characteristic of the cold dark matter (CDM) hypothesis is the presence of a very large number of low-mass haloes, too small to have made a visible galaxy. Other hypotheses for the nature of the dark matter, such as warm dark matter (WDM), predict a much smaller number of such low-mass haloes. Strong lensing systems offer the possibility of detecting small-mass haloes through the distortions they induce in the lensed image. Here, we show that the main contribution to the image distortions comes from haloes along the line of sight rather than subhaloes in the lens as has normally been assumed so far. These interlopers enhance the differences between the predictions of CDM and WDM models. We derive the total perturber mass function, including both subhaloes and interlopers, and show that measurements of approximately 20 strong lens systems with a detection limit of  $M_{\text{low}} = 10^7 h^{-1} M_{\odot}$  would distinguish (at  $3\sigma$ ) between CDM and a WDM model consisting of 7 keV sterile neutrinos such as those required to explain the recently detected 3.5 keV X-ray emission line from the centres of galaxies and clusters.

**Key words:** gravitational lensing: strong – galaxies: haloes – dark matter.

## 1 INTRODUCTION

Under the cold dark matter (CDM) hypothesis, the power spectrum of linear density perturbations has power on all scales down to a very small cutoff which depends on the nature of the cold particles but is typically of the order of Earth mass (Green, Hofmann & Schwarz 2005). As a result, the mass function of CDM haloes increases roughly as a power law to low masses (Diemand et al. 2008; Springel et al. 2008b) and the defining characteristic of a CDM universe is the existence of a very large number of low-mass haloes. Most of these are too small for gas to have cooled in them to form visible galaxies (e.g. Efstathiou 1992; Benson et al. 2002; Sawala et al. 2016b).

Alternative candidates for the dark matter such as sterile neutrinos behave as warm dark matter (WDM). Their free streaming in the early universe erases perturbations much larger than the Earth mass, typically on the scale of dwarf galaxies. As a result, these models predict far fewer small-mass haloes than CDM and none at all below the corresponding cutoff mass in the power spectrum which also depends on the properties of the particles (e.g. Avila-Reese et al. 2003; Lovell et al. 2012, 2016; Schneider et al. 2012; Kang, Macciò & Dutton 2013; Bose et al. 2016; Wang et al. 2016). A particularly topical candidate of this kind is a sterile neutrino of mass of 7 keV whose decay could explain the 3.5 keV line recently

detected from the centres of galaxies and clusters (Bulbul et al. 2014; Boyarsky et al. 2014). In the ‘coldest’ example of a 7 keV sterile neutrino, the cutoff occurs at a mass of a few times  $10^8 h^{-1} M_{\odot}$  (Bose et al. 2016).

CDM and viable WDM models predict similar numbers of faint dwarf galaxies such as those observed as satellites around the Milky Way (Kennedy et al. 2014; Lovell et al. 2015). Although the recent discovery of new satellites may rule out some currently acceptable WDM models (Bose et al. 2017), a definitive test of WDM and, indeed, of CDM, requires searching for the even smaller haloes which failed to make a galaxy and thus remain dark. Analyses of strong lensing systems offers the possibility of achieving exactly this. Koopmans (2005) and Vegetti & Koopmans (2009a) showed that small haloes projected on to an Einstein ring or giant arc cause a potentially detectable distortion of the image and Vegetti & Koopmans (2009b) showed that a Bayesian analysis of sufficiently deep photometric data can be used to constrain the subhalo mass function (SHMF; see also Vegetti et al. 2012, 2014; Hezaveh et al. 2016; Minor, Kaplinghat & Li 2016).

The technique proposed by Vegetti & Koopmans (2009a) has already returned the detection of a halo of mass  $1.9 \pm 10^8 h^{-1} M_{\odot}$  in the Einstein ring of JVAS B1938+666 (Vegetti et al. 2012). These authors claim that with imaging data of similar quality the detection sensitivity can reach  $2 \times 10^7 h^{-1} M_{\odot}$ . In a recent paper (Li et al. 2016), we showed that observations of approximately 100 strong lens systems with a detection limit of  $M_{\text{low}} = 10^7 h^{-1} M_{\odot}$  could, in principle, distinguish CDM for even the coldest 7 keV

\* E-mail: [liran827@gmail.com](mailto:liran827@gmail.com)

sterile neutrino dark matter model. Of course, failure to detect haloes of such low mass would conclusively rule out CDM altogether.

A common assumption made in studies of strong lensing is that the haloes that perturb the image lie at the same redshift as the main lens, i.e. that they are subhaloes of the lens. However, it is possible that the large number of haloes along the line of sight to a lens could be the dominant source of distortion of the lensed image. Many previous studies have shown that the line-of-sight haloes can play an important role in the modelling of lensed quasar systems (e.g. Chen, Kravtsov & Keeton 2003; Metcalf 2005; Wambsganss, Bode & Ostriker 2005; Xu et al. 2009). In this paper, we calculate the contribution of these ‘interlopers’ and investigate how they affect the prospects of distinguishing different dark matter candidates.

Since the majority of the distortions are produced by dark haloes and subhaloes, at first sight baryon effects may seem to be irrelevant. However, this is not quite true, i.e. the visible galaxy at the centre of the lens can, in principle, destroy dark subhaloes by dynamical effects such as tidal stripping. In this paper, we neglect baryon effects but we investigate those in a companion paper using the APOSTLE hydrodynamic simulations (Sawala et al. 2016a).

The paper is organized as follows. In Section 2, we calculate the number density of line-of-sight haloes both in CDM and WDM models using the respective halo mass functions. In Section 3, we estimate the effect of individual interlopers and derive the effective perturber mass functions. In Section 4, we illustrate the constraining power of halo/subhalo detection from multiple lens systems when including interlopers. Our conclusions are summarized in Section 5.

## 2 NUMBER DENSITY OF HALOES ALONG THE LINE OF SIGHT

Let  $\theta_E$  be the Einstein radius of a lens. The light rays that cross an annulus of thickness of  $2\delta\theta$  around the lens form a light cone whose volume is given by

$$V = \int_0^{z_s} \pi [R(z, \theta_E + \delta\theta)^2 - R(z, \theta_E - \delta\theta)^2] \frac{d\chi(z)}{dz} dz, \quad (1)$$

where  $\chi(z)$  is the comoving distance from the observer at redshift 0 to redshift  $z$  and  $R(z, \theta)$  is the transverse distance corresponding to angle  $\theta$  at redshift  $z$ . When  $z < z_l$ ,  $R(z, \theta)$  is simply  $D(0, z)\theta$ , where  $D(0, z)$  is the comoving distance from the observer to redshift  $z$ . When  $z > z_l$ ,  $R(z, \theta) = D(0, z)\theta - \hat{\alpha}D(z_l, z)$  (see the sketch in Fig. 1), where  $\hat{\alpha}$  is the deflection angle of the lens. Thus,  $R(z, \theta)$  may be written as

$$R(z, \theta) = \begin{cases} \theta D(0, z), & z < z_l \\ \theta D(0, z) - \hat{\alpha}D(z_l, z), & z > z_l. \end{cases} \quad (2)$$

For a singular isothermal sphere (SIS) lens,  $\hat{\alpha} = \theta_E D(0, z_s)/D(z_l, z_s)$  is a constant. The total number of haloes in the light cone with mass in the range,  $[M_1, M_2]$ , is given by

$$N_{\text{los}}(\theta_E, \delta\theta) = \int_0^{z_s} n(M_1, M_2, z) \frac{dV}{dz} dz, \quad (3)$$

where

$$n(M_1 < m < M_2, z) = \int_{M_1}^{M_2} \frac{dn(m, z)}{dm} dm, \quad (4)$$

where  $dn(m, z)/dm$  is the halo mass function at redshift  $z$ .

In Fig. 2, we compare the projected number density of interlopers and lens subhaloes in the Einstein ring region for a lens in a CDM

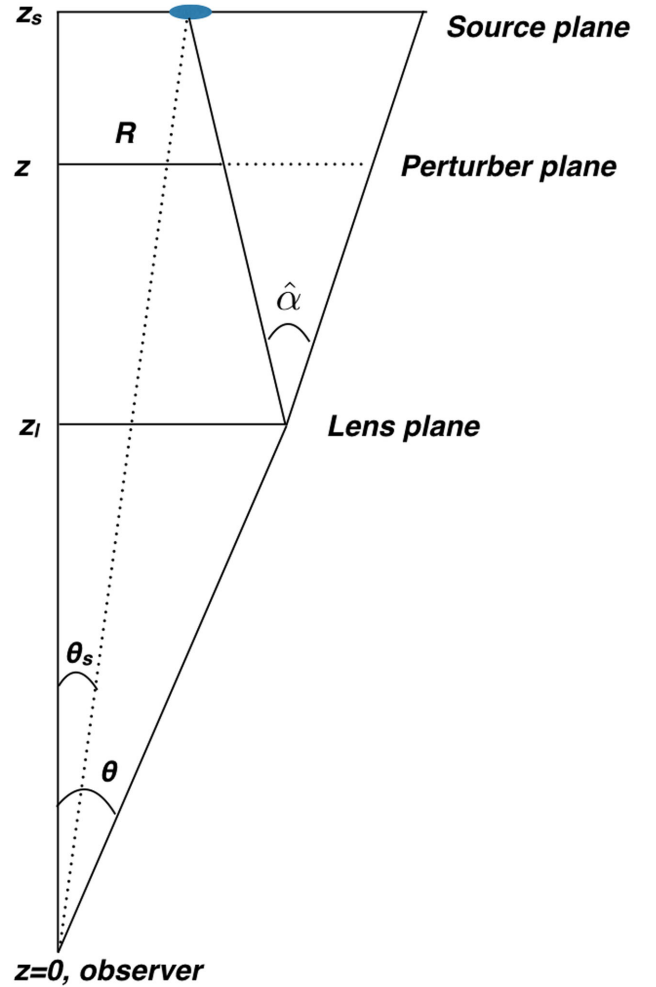


**Figure 1.** Geometry of the source/lens/observer system.  $\theta_s$  is the position of the source and  $\theta$  is the position of the image.  $R(z, \theta)$  is the transverse distance corresponding to angle  $\theta$  at redshift  $z$ . When  $z < z_l$ ,  $R(z, \theta)$  is simply  $D(0, z)\theta$ , where  $D(0, z)$  is the comoving distance from observer to redshift  $z$ , while if  $z > z_l$ ,  $R(z, \theta) = D(0, z)\theta - \hat{\alpha}D(z_l, z)$ .

halo of mass  $10^{13} h^{-1} M_\odot$  at  $z_l = 0.2$ . To calculate the number density of interlopers we use the formula for the halo mass function proposed by Sheth & Tormen (1999). We use the projected number density of subhaloes derived by Xu et al. (2015) from the Phoenix and Aquarius  $N$ -body simulations (Springel et al. 2008a; Gao et al. 2011). The projected number density of line-of-sight dark matter haloes is larger than that of subhaloes associated with the lens by a factor of 2–5.

The corresponding projected number densities for a WDM model are also shown in Fig. 2. This model comes from the high-resolution COCO-WARM simulation, the WDM run of the Copernicus Complexio project (Bose et al. 2016, 2017; Hellwing et al. 2016), which corresponds to a thermal WDM particle of mass 3.3 keV. This is indistinguishable from a sterile neutrino model of mass 7 keV with leptogenesis parameter,  $L_6 = 8.66$  which corresponds to the coldest sterile neutrino model consistent with the dark matter decay interpretation of the 3.5 keV X-ray line (Lovell et al. 2016). Ruling out this extreme model would exclude the entire family of 7 keV sterile neutrinos.

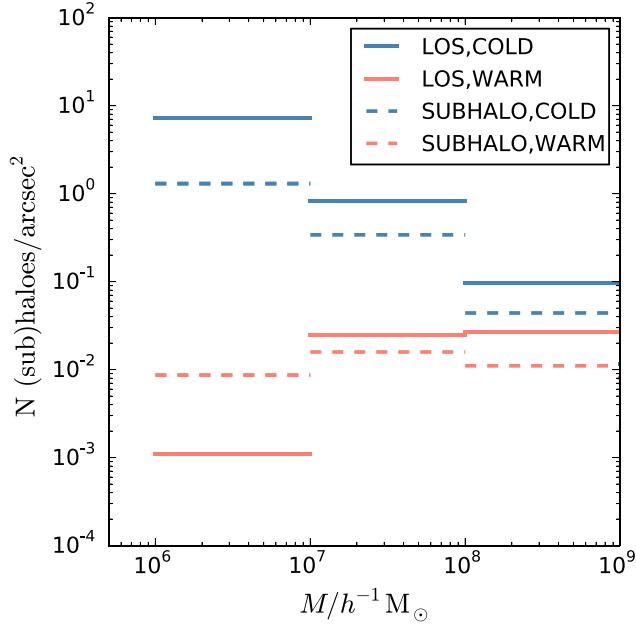


**Figure 2.** Relative contributions of lens subhaloes and interlopers. The dashed bars show the projected number density of subhaloes in the Einstein ring region of a lens in a halo of  $10^{13} h^{-1} M_{\odot}$  at redshift  $z_1 = 0.2$ . The solid bars show the projected number density in that region of line-of-sight haloes. Blue and black lines are for CDM and red for WDM, as indicated in the legend. The width of the bars shows the range of each mass bin. The projected subhalo number density is calculated with equation (8).

### 3 THE NUMBER DENSITY OF PERTURBING INTERLOPERS

The lensing effect of an interloper halo projected on to the Einstein ring of a lens depends on its mass, structure and redshift. There is a strong degeneracy between mass and redshift. In this section, we calculate the lensing effect of interlopers by creating mock Einstein ring images using ray-tracing simulations. The mass model for the lens plus perturber consists of a main lens and a halo along the line of sight.

We assume that the main lens is at  $z_1 = 0.2$  and has a SIS profile with  $\sigma_v = 350 \text{ km s}^{-1}$ . An interloper of mass  $M_{\text{int}} = 5 \times 10^6 h^{-1} M_{\odot}$  is placed at  $z_{\text{int}} = 0.18$  and a Gaussian source is placed at redshift  $z_1 = 1.0$ . The perturber density profile is assumed to have the NFW form (Navarro, Frenk & White 1997) with concentration given by the median of the mass–concentration relation of Neto et al. (2007). The brightness distribution of the source galaxy is assumed to be Gaussian with dispersion  $\sigma_{\text{source}} = 0.05 \text{ arcsec}$ .

We then use a ray-tracing code to generate a lensed image on a plane of  $500 \times 500$  pixels. The size of each pixel is  $0.043 \text{ arcsec}$ , which is close to the *Hubble* telescope imaging resolution. We assume that the uncertainty in the flux in each pixel is 10 per cent of the mean flux. Once a mock image has been generated, we use an MCMC minimization method to fit the image with the same mass model as above in which all parameters, except the redshift,  $z_{\text{int}}$ , and mass,  $M_{\text{int}}$ , of the interlopers are fixed.

The posterior distribution of  $z_{\text{int}}$  and  $M_{\text{int}}$ , displayed in Fig. 3, clearly shows that these two parameters are highly degenerate with the  $1\sigma$  contour including a very wide range of redshifts and masses. A low-mass interloper in front of the lens can have a similar lensing effect as a higher mass interloper behind the lens. Since the halo mass function increases with decreasing mass, the higher the lens

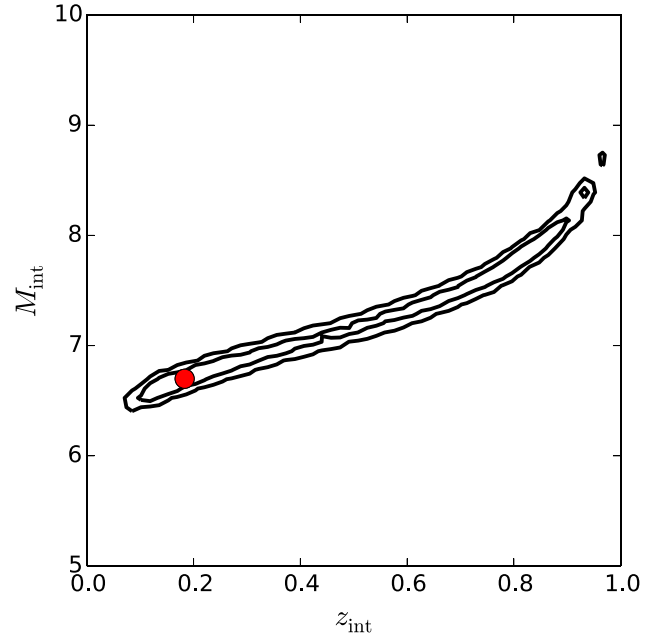


**Figure 3.** The posterior distribution of interloper mass,  $M_{\text{int}}$ , and redshift,  $z_{\text{int}}$  for an interloper of mass of  $5 \times 10^6 h^{-1} M_{\odot}$  placed at  $z = 0.18$ . The contours show the 68 per cent and 95 per cent confidence levels. There is a clear degeneracy between  $z_{\text{int}}$  and  $M_{\text{int}}$ . We have assumed a flux uncertainties of 10 per cent of the mean flux.

redshift, the more important interlopers become. We find that within a small range of the Einstein radius, the form of the degeneracy between  $z_{\text{int}}$  and  $M_{\text{int}}$  is independent of the angular position of the interloper.

If we fix the interloper redshift to be  $z_{\text{lens}}$  during the fitting, we can derive a best-fitting ‘effective mass’,  $M_{\text{eff}}(M_{\text{int}}, z_{\text{int}}, \theta)$ , where  $M_{\text{int}}$  and  $z_{\text{int}}$  are the true mass and redshift of the interloper, and  $\theta$  is its angular position. In other words, we can use a subhalo of  $M_{\text{eff}}$  at redshift  $z_{\text{lens}}$  to model an image perturbation caused by an interloper of mass  $M_{\text{int}}$  at redshift  $z_{\text{int}}$ .

Note that, in this ray-tracing test, we do not include observational details such as the point spread function (PSF), source complexity or noise variation across the image. If an interloper with mass,  $M_{\text{int}}$ , and redshift,  $z_{\text{int}}$ , has the same lensing effect as a subhalo of mass,  $M_{\text{eff}}$ , in this idealized simulation, it should have the same lensing effect as a subhalo of  $M_{\text{eff}}$  in a more realistic simulation with PSF and noise added. Our idealized ray-tracing simulation therefore encapsulates the key information regarding the mass–redshift degeneracy inherent in the modelling of the perturber.

We assume that the mass detection limit for subhaloes is  $M_{\text{low}}$  within a thin annulus of thickness  $\delta\theta$  around the Einstein radius. Then, any interlopers with  $M_{\text{eff}} > M_{\text{low}}$  can be detected. We refer to these as ‘perturbing interlopers’. The projected number density of perturbing interlopers can be written as

$$\begin{aligned} \Sigma_{\text{pb}}(>M_{\text{low}}) &= \frac{1}{\theta_E \delta\theta} \int_0^{z_s} n(M_{\text{int,low}} < m < M_{\text{max}}, z) \mathcal{R}(z, \theta_E) \delta R(z, \delta\theta) \frac{d\chi(z)}{dz} dz, \end{aligned} \quad (5)$$

where  $M_{\text{int,low}}$  is defined implicitly by  $M_{\text{eff}}(M_{\text{int,low}}, z) = M_{\text{low}}$ ,  $M_{\text{max}} = 10^{11} h^{-1} M_{\odot}$  is a cutoff mass we impose for the maximum halo mass considered for the mass function in the volume along the

line of sight to the lens. The number density of haloes is dominated by the low-mass end, the exact choice of  $M_{\max}$  has no effect on the results.

The projected subhalo number density in a CDM universe can be written as

$$\Sigma_{\text{sub,cdm}}(m) = \Sigma_0 \left( \frac{m}{h^{-1}M_{\odot}} \right)^{-\alpha}, \quad (6)$$

and the cumulative surface density of subhaloes in the mass range,  $[M_1, M_2]$ , can be written as

$$\Sigma_{\text{sub,cdm}}(M_1 < m < M_2) = \begin{cases} \Sigma_0 \ln \frac{M_2}{M_1} & \text{if } \alpha = 1, \\ \frac{\Sigma_0}{1-\alpha} (M_2^{1-\alpha} - M_1^{1-\alpha}) & \text{otherwise.} \end{cases}$$

According to Fig. 2, the projected number density of subhaloes with mass  $10^6$ – $10^7 h^{-1} M_{\odot}$  is  $1.3 \text{ arcsec}^{-2}$ . Thus, we have  $\Sigma_0 = 3.1 \times 10^5 \text{ arcsec}^{-2}$ , assuming  $\alpha = 1.9$ .

Following Schneider et al. (2012) and Lovell et al. (2014), we write the SHMF as

$$\frac{d\Sigma_{\text{sub,wdm}}}{dm} = \frac{d\Sigma_{\text{sub,cdm}}}{dm} (1 + m_c/m)^{-\beta}, \quad (7)$$

and the cumulative mass function,  $\Sigma_{\text{sub,wdm}}(M_1, M_2)$ , can be written as

$$\Sigma_{\text{sub,wdm}} = \frac{\Sigma_0}{1 - \alpha + \beta} [F(M_2, \alpha, \beta, m_c) - F(M_1, \alpha, \beta, m_c)], \quad (8)$$

where

$$F(x, \alpha, \beta, m_c) = \frac{x^{1-\alpha+\beta}}{m_c^{\beta}} {}_2F_1 \left( \beta, 1 - \alpha + \beta, 2 - \alpha + \beta, \frac{-x}{m_c} \right). \quad (9)$$

Here  ${}_2F_1$  is the hypergeometric function. In the COCO-WARM simulation,  $\beta = 1.3$  and  $m_c = 1.3 \times 10^8 h^{-1} M_{\odot}$  (Li et al. 2016).

Fig. 4 shows the cumulative number density of perturbing interlopers in CDM and in the WDM model of COCO-WARM. For comparison, we overplot the projected number density of subhaloes in a host halo of  $10^{13} h^{-1} M_{\odot}$  at redshift  $z_1 = 0.2$ . Fig. 4 shows that for both CDM and WDM, the perturbing interlopers dominate the distortions in the Einstein ring image. In the CDM case, the projected number density of perturbing interlopers is  $\sim 3$  times the number density of lensing subhaloes. In the COCO-WARM case, the excess is a factor of 2 at  $M = 10^9 h^{-1} M_{\odot}$ , but decreases to 50 per cent at  $M = 10^6 h^{-1} M_{\odot}$ . Thus, the interlopers act to magnify the difference in the number of detectable perturbers in the two cases. The different boost factors between CDM and WDM are due to the differences in the shapes of the halo mass function in the two models. The total perturber mass function is an integral over all perturbing interlopers and perturbing subhaloes. In a CDM universe, the mass function over the mass range of interest follows a power law whose index is very similar to that of the SHMF. The total perturber mass function is then just boosted by a constant factor. The halo and SHMFs in the WDM model both have a mass cutoff at about  $10^8 h^{-1} M_{\odot}$ . The detection limit for interloper haloes varies with redshift so, in this case, the total perturber mass function does not have exactly the same shape as the SHMF.

#### 4 CONSTRAINTS ON THE IDENTITY OF DARK MATTER

As we have seen, to predict correctly the distortions in the Einstein ring image it is necessary to model the total perturber

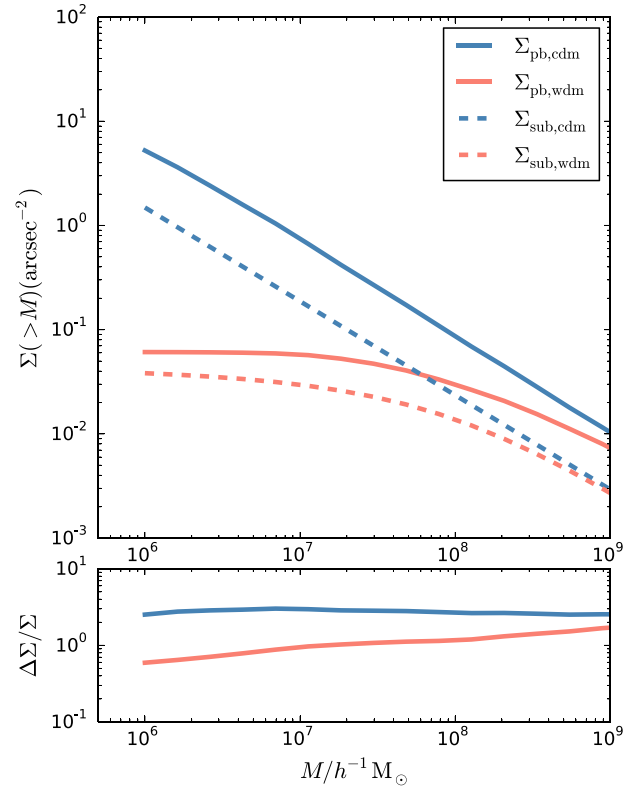


**Figure 4.** Cumulative number densities of perturbing interlopers and subhaloes and as a function of the subhalo mass detection limit. The blue dashed line gives the number density of subhaloes of mass greater than  $M_{\text{low}}$  in a host halo of mass of  $10^{13} h^{-1} M_{\odot}$  at redshift 0.2, derived by Xu et al. 2015. The red dashed line gives the corresponding number density of subhaloes in the COCO-WARM simulation. The blue and red solid lines show the number density of perturbing interlopers along the line of sight in the CDM and COCO-WARM cases, respectively. The lower panel shows  $[\Sigma_{\text{pb}}(>M) - \Sigma_{\text{sub}}(>M)]/\Sigma_{\text{sub}}(>M)$ .

surface density,  $\Sigma_{\text{tot}} = \Sigma_{\text{sub}} + \Sigma_{\text{pb}}$ , which includes both interlopers and subhaloes in the lens. We find that the total surface density of perturbers in the CDM and WDM models can be described by a formula of the form of equations (6) and (7), respectively. For CDM,  $\Sigma_{\text{tot}}$  can be used with  $\alpha = 1.9$  and  $\log \Sigma_0 = 6.2$ , and for COCO-WARM,  $\Sigma_{\text{tot}}$  can be used with  $\alpha = 1.9$ ,  $\log \Sigma_0 = 6.1$ ,  $\beta = 1.3$  and  $\log(m_c/h^{-1} M_{\odot}) = 8.3$ . We can then exploit the difference in the perturber mass functions to attempt to constrain the identity of dark matter. Here, the key parameter is  $m_c$  which describes the cutoff mass for the perturber mass function in the WDM model.

To explore the constraining power of a detection of strong lensing perturbations we adopt a similar methodology to that introduced by Li et al. (2016). First, we generate mock subhalo detections using the following Monte Carlo method.

We fix the lens and source redshifts to be  $z_1 = 0.2$  and  $z_s = 1.0$ , respectively, and assume that the lens galaxy is a SIS with velocity dispersion,  $\sigma_v = 350 \text{ km s}^{-1}$ , which is similar to those of the most massive lenses in the Sloan Lens ACS Survey (SLACS, Bolton et al. 2006) lens sample.

For each lens, we randomly sample subhaloes and perturbing interlopers around the Einstein ring region according to their mass functions.

Following Li et al. (2016) and Vegetti & Koopmans (2009b), we assume that only perturbers that fall in a thin annulus around

the Einstein radius of width  $2\delta\theta = 0.6$  arcsec can be detected. We consider two different detection limits,  $M_{\text{low}} = 10^8 h^{-1} M_{\odot}$ , the best current limit using *HST* imaging (Vegetti et al. 2014), and  $10^7 h^{-1} M_{\odot}$ , the detection limit that can be reached using laser guide star adaptive optics imaging with Keck (Vegetti et al. 2012) or a next generation telescope like the TMT or VLBI (McKean et al. 2015; Skidmore, TMT International Science Development Teams & Science Advisory Committee 2015). We assume that each subhalo detection has a Gaussian measurement error with standard deviation,  $\sigma_m = M_{\text{low}}/3$ . We generate two sets of mock detection catalogues, with the mass functions appropriate to CDM and COCO-WARM, respectively.

We then perform an MCMC fit for each mock detection catalogue. There are four free parameters in the model:  $\alpha$ ,  $\Sigma_0$ ,  $\beta$  and  $m_c$ . Given these model parameters, the mean number of detected subhaloes can be written as

$$\begin{aligned} \mu(\alpha, \beta, m_c, \Sigma_0) \\ = 4\pi\theta_E^2 \delta\theta \int_{M_{\text{low}}}^{\infty} \int_{M_{\text{min}}}^{M_{\text{max}}} \frac{d\Sigma_{\text{tot}}}{dm} \frac{1}{\sqrt{2\pi}\sigma_m} \exp\left[-\frac{(m-m')^2}{2\sigma_m^2}\right] dm' dm. \end{aligned} \quad (10)$$

The likelihood of finding a set of  $n_s$  subhaloes of masses,  $\mathbf{m} \equiv \{m_1, m_2, \dots, m_{n_s}\}$ , in one Einstein ring system is then given by

$$\mathcal{L}(n_s, \mathbf{m} | \mathbf{p}, \mathbf{q}) = \frac{e^{-\mu} \mu^{n_s}}{n_s!} \prod_{i=1}^{n_s} P(m_i | \mathbf{p}, \mathbf{q}), \quad (11)$$

where the vector,  $\mathbf{p} = \{\Sigma_0, \alpha, \beta, m_c\}$ , contains the parameters of the model and the vector,  $\mathbf{q} = \{M_{\text{min}}, M_{\text{max}}, M_{\text{low}}\}$ , contains the values of the parameters that define the minimum and maximum masses cutoff we consider for the perturber mass function and the mass detection limit. The parameters,  $\mathbf{q}$ , are fixed during the fitting process. In this process, we set  $M_{\text{min}} = 10^6$  and  $M_{\text{max}} = 10^{11} h^{-1} M_{\odot}$ . The exact choice of  $M_{\text{min}}$  and  $M_{\text{max}}$  does not affect the results.

The term  $P(m_i | \mathbf{p}, \mathbf{q})$  gives the probability density of detecting a subhalo of measured mass,  $m_i$ :

$$P(m_i | \mathbf{p}, \mathbf{q}) = \frac{\int_{M_{\text{min}}}^{M_{\text{max}}} \frac{d\Sigma_{\text{tot}}}{dm} \exp\left[-\frac{(m_i-m')^2}{2\sigma_m^2}\right] dm'}{\int_{M_{\text{low}}}^{M_{\text{max}}} \int_{M_{\text{min}}}^{M_{\text{max}}} \frac{d\Sigma_{\text{tot}}}{dm} \exp\left[-\frac{(m-m')^2}{2\sigma_m^2}\right] dm' dm}. \quad (12)$$

The denominator in this equation is a normalization factor. The total likelihood for  $N$  lenses may be written as

$$\mathcal{L}_{\text{tot}} = \prod_{j=0}^N \mathcal{L}(n_j, \mathbf{m}_j | \mathbf{p}, \mathbf{q}), \quad (13)$$

where  $n_j$  and  $\mathbf{m}_j$  are the number and masses of the perturbers detected in the  $j$ th system.

Following Li et al. (2016), we adopt a Gaussian prior for  $\alpha$  with expectation 1.9 and standard deviation 0.1, and a Gaussian prior for  $\beta$  with expectation 1.3 and standard deviation 0.1. We adopt flat priors for  $\log(\Sigma_0)$  and  $\log(m_c/h^{-1} M_{\odot})$  in the ranges [1, 10] and [4, 11], respectively.

Fig. 5 shows the posterior distributions of  $\Sigma_{\text{tot}}(>M_{\text{low}})$ , and the cutoff mass,  $m_c$ . The upper panels are for  $N = 20$  lenses and the lower panels for  $N = 100$  lenses. In both cases, the detection limit is assumed to be  $M_{\text{low}} = 10^7 h^{-1} M_{\odot}$ . The left-hand panel shows the result for our CDM mock catalogues and the right-hand panel for the COCO-WARM case.

Encouragingly, we find that a detection limit of  $10^7 h^{-1} M_{\odot}$  is sufficient to distinguish between the two dark matter models. If we live in a CDM universe (left-hand panel), with a sample of only

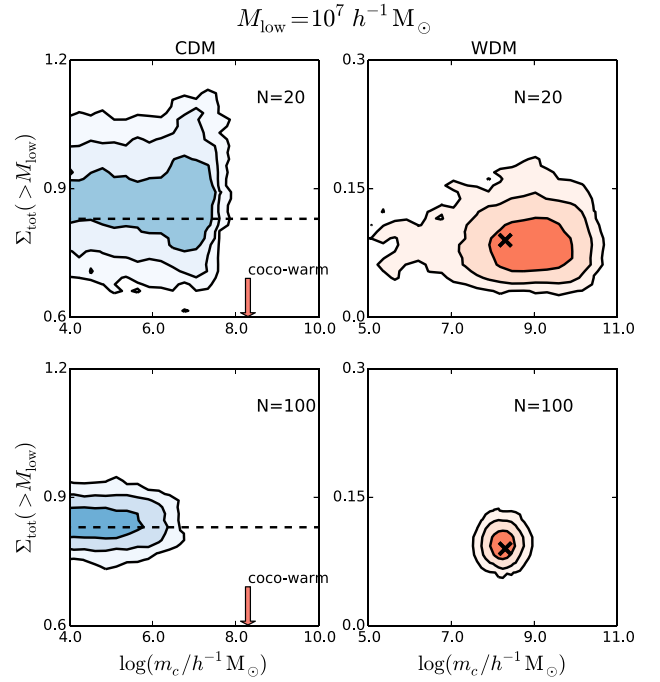


**Figure 5.** The posterior distribution of  $\Sigma_{\text{tot}}(>M_{\text{low}})$ ; in units of  $\Sigma_{\text{tot}}$  arcsec $^{-2}$  and perturber mass function cutoff mass,  $m_c$ . The contours indicate the 67 per cent, 95 per cent and 99.7 per cent confidence levels. The left-hand panels show results for CDM while the right-hand panels show results for the COCO-WARM model. The upper panels are for  $N = 20$  and the lower panels for  $N = 100$  lenses. The detection limit is assumed to be  $M_{\text{low}} = 10^7 h^{-1} M_{\odot}$ . In the right-hand panels, the crosses show the input values of  $m_c$  and  $\Sigma_{\text{tot}}$  and in the left-hand panels, the dashed lines indicate the input value of  $\Sigma_{\text{tot}}$ . The arrows mark the value of  $m_c$  for the COCO-WARM model.

20 lenses we are able to rule out  $\log(m_c/h^{-1} M_{\odot}) = 8.3$  at the  $3\sigma$  level. By contrast, if we live in a universe in which the dark matter consists of 7 keV sterile neutrinos (right-hand panel), with  $N = 20$  lenses and  $M_{\text{low}} = 10^7 h^{-1} M_{\odot}$  we can rule out, at the  $3\sigma$  level, all dark matter models with  $\log(m_c/h^{-1} M_{\odot}) < 5$ , which, of course, includes CDM! The constraining power increases with the number of lens systems. If the number is 100, and the dark matter is as in COCO-WARM, we can rule out all dark matter models with  $\log(m_c/h^{-1} M_{\odot}) < 7.5$  at  $3\sigma$ .

Fig. 6 shows the constraints on  $m_c$  and  $\Sigma_{\text{tot}}$  that can be obtained for the COCO-WARM model with  $N = 100$  and  $M_{\text{low}} = 10^8 h^{-1} M_{\odot}$ . Dark matter models with  $m_c > 10^9 h^{-1} M_{\odot}$  are disfavoured, but the CDM model cannot be ruled out by this experiment. This agrees with the conclusion of Li16 that the constraining power on  $m_c$  is weaker when the detection limit,  $M_{\text{low}} > 10^8 h^{-1} M_{\odot}$ . Above this mass, the slope of the mass function of perturbers in the COCO-WARM model is intrinsically similar to that of CDM. On the other hand, with  $N = 100$ , one can place a tight constraint on  $\Sigma_{\text{tot}}$  which would provide a strong hint that the dark matter is not CDM since, as we can see in the figure, the best-fitting  $\Sigma_{\text{tot}}$  is far below the prediction of a CDM universe. This demonstrates that the identity of the dark matter can be strongly constrained by the total number of perturbations alone.

In this paper, we have assumed a lens model with  $\sigma_v = 350$  km s $^{-1}$  and  $z_s = 1$ , which is near the upper envelope of the SLACS sample. More massive lenses, in combination with more distant sources, produce larger Einstein rings and these lead to larger volumes for

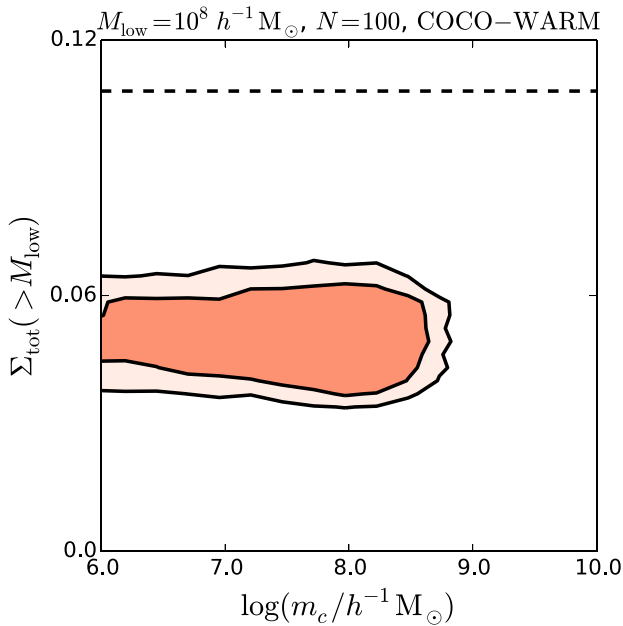


**Figure 6.** Same as Fig. 5, but for a detection threshold,  $M_{\text{low}} = 10^8 h^{-1} M_{\odot}$ , and a number of lenses,  $N = 100$ . The input perturber mass function is from the COCO-WARM model. The black dashed line shows the expected value of  $\Sigma_{\text{tot}}$  in CDM.

interloper detection. These lenses should be high-priority targets for future high-resolution observations. If we adopt a configuration similar to the average SLACS sample, with  $z_1 = 0.7$  and  $\sigma_v = 275 \text{ km s}^{-1}$  (Bolton et al. 2006), we require 50 per cent more lenses to achieve similar constraining power.

An important simplification we have made is to assume a uniform detection limit for the perturber over the entire Einstein ring. In a real situation, the detection limit varies across the Einstein ring region and a sensitivity map that specifies the subhalo mass detection limit at each pixel of the image, like those made by Vegetti et al. (2014), is crucial for constraining the perturber mass function. Once such a map has been constructed, the strategy used in this paper can be applied with minor changes. In particular, in equations (11)–(13), one should first calculate the likelihood of detecting  $n_s$  perturbers in the  $i$ th pixel of the  $j$ th lens and then sum the likelihood over all the pixels of all lenses.

In this study, we have also neglected the effects of the galaxy in the lens on the population of subhaloes orbiting in the same halo. In a recent paper, Sawala et al. (2016a) calculated the changes in the abundance and spatial distribution of subhaloes in the mass range  $10^{6.5}–10^{8.5} h^{-1} M_{\odot}$ , in haloes of mass of  $10^{12} h^{-1} M_{\odot}$ , caused by interaction with the central galaxy. By comparing the hydrodynamical simulations of the APOSTLE project of Local Group simulations with their dark matter only counterparts, they found the reduction in the number of subhaloes as a function of radial distance due to tidal disruption in the potential well deepened by the presence of the central galaxy to be approximately independent of subhalo mass. At halocentric distances  $r < 50 \text{ kpc}$ , the number of subhaloes is reduced by  $\sim 40$ – $50$  per cent and at radii in the range  $r = 50$ – $200 \text{ kpc}$  by 23 per cent.

The host haloes in the APOSTLE simulations are an order of magnitude less massive than the haloes we are considering in this study. If we assume that the reduction in numbers scales with  $r/r_{200}$ , we should expect the number of subhaloes in strong lenses system

also to be  $\sim 20$ – $50$  per cent smaller than the number predicted in dark matter only simulations. This effect, however, does not alter the conclusions in this paper because, as we have seen, the perturbers of Einstein ring systems are predominantly field haloes along the line of sight to the lens, rather than subhaloes.

## 5 SUMMARY

The most direct, and potentially conclusive, test of different models for the dark matter is to measure the mass function of dark matter haloes in the low-mass regime where different models that agree with cosmic microwave background and large-scale structure data can be expected to differ. Unfortunately, attempts to infer the small-mass end of the dark halo mass function from observations of visible galaxies are hampered by the intrinsically low luminosity of faint objects and further complicated by uncertainties in modelling baryon effects.

In contrast Einstein rings (and giant arcs) produced by strong gravitational lensing, offer a clean and powerful means to detect small haloes and measure or constrain the halo mass function. These small haloes perturb lensed images and by modelling these perturbations, it is possible to detect individual haloes projected on to the image and measure their mass. There is a strong degeneracy between the mass of a perturber and its redshift. As a result, the lensing effect of an interloper halo along the line of sight can be modelled as that produced by a (sub)halo of some effective mass located at the redshift of a lens.

In this paper, we have compared the CDM model with a WDM model whose linear perturbation power spectrum is that of a thermally produced 3.3 keV particle and provides a very good approximation to the linear power spectrum of the coldest possible 7 keV sterile neutrino consistent with a particle decay interpretation of the recently discovered 3.5 keV line in the X-ray spectra of galaxies and clusters. Ruling out this model by detecting small haloes below the cutoff mass in its predicted halo mass function would rule out all 7 keV sterile neutrino models. Similarly, a failure to detect small-mass subhaloes would rule out CDM.

For both CDM and WDM models, we have calculated the projected number density of interlopers and compared it to the projected number of subhaloes. We defined the ‘perturbing’ interlopers as those that generate a larger lensing signal than a subhalo of mass,  $M_{\text{low}}$ . We then derived the effective mass function of perturbers, including both perturbing interlopers and subhaloes. We find that the total number density of perturbers is four times of that of subhaloes in CDM and 1.5–2 times of that of subhaloes in our WDM model. Interlopers therefore boost the probability of detection and act to magnify the difference between CDM and WDM.

We find that a measurement of only 20 strong lensing systems with a detection threshold of  $M_{\text{low}} = 10^7 h^{-1} M_{\odot}$  is enough to distinguish between CDM and our WDM model at the  $2\sigma$  level. With a survey of 100 strong lenses the confidence level increases to  $3\sigma$ . If the threshold mass,  $M_{\text{low}} = 10^8 h^{-1} M_{\odot}$ , the constraint on the cutoff halo mass of our WDM model,  $m_c$  becomes weaker because the slope of the effective mass function above  $10^8 h^{-1} M_{\odot}$  in this model is similar to that in CDM but the constraint on the total number density of perturbers is tight, thus retaining discriminating power between the models.

Strong gravitational lensing provides, in principle, a clean test of dark matter models. The quality of existing data and analysis technique is already sufficient to detect dark low-mass haloes, too small to have made a galaxy. As a result this technique is almost unaffected by uncertain baryon effects, except for the possibility

that the disruption of subhaloes orbiting within a large halo may be enhanced by the concentration of mass induced by the central galaxy. This kind of processes can be quantified with hydrodynamic simulations and, once this is achieved, as we shown a conclusive test of the nature of the dark matter will be possible. In particular lensing measurements forthcoming in the next few years offer the possibility of ruling out the main current candidates for the dark matter, CDM and WDM.

## ACKNOWLEDGEMENTS

RL acknowledges NSFC grant (Nos. 11303033, 11511130054, 11333001), support from the Newton Fund, Youth Innovation Promotion Association of CAS and YIPA of NAOC. CSF and SMC acknowledge the European Research Council Advanced Investigator grant, GA 267291, COSMIWAY. LG acknowledges support from the NSFC grant (Nos. 11133003, 11425312), the Strategic Priority Research Program, The Emergence of Cosmological Structure of the Chinese Academy of Sciences (No. XDB09000000) and a Newton Advanced Fellowship, as well as the hospitality of the Institute for Computational Cosmology at Durham University. This work was supported by the Consolidated Grant [ST/L00075X/1] to Durham from the Science and Technology Facilities Council. This work used the DiRAC Data Centric system at Durham University, operated by the Institute for Computational Cosmology on behalf of the STFC DiRAC HPC Facility ([www.dirac.ac.uk](http://www.dirac.ac.uk)). The DiRAC system is funded by BIS National E-infrastructure capital grant ST/K00042X/1, STFC capital grant ST/H008519/1, STFC DiRAC Operations grant ST/K003267/1 and Durham University. DiRAC is part of the National E-Infrastructure. We thank the participants of the workshop ‘Dark matter on the smallest scale’ (Lorentz Centre – 2016 April 4–8) for lively discussions and Simon White for his insightful comments.

## REFERENCES

- Avila-Reese V., Colín P., Piccinelli G., Firmani C., 2003, *ApJ*, 598, 36  
 Benson A. J., Frenk C. S., Lacey C. G., Baugh C. M., Cole S., 2002, *MNRAS*, 333, 177  
 Bolton A. S., Burles S., Koopmans L. V. E., Treu T., Moustakas L. A., 2006, *ApJ*, 638, 703  
 Bose S., Hellwing W. A., Frenk C. S., Jenkins A., Lovell M. R., Helly J. C., Li B., 2016, *MNRAS*, 455, 318  
 Bose S., Hellwing W. A., Frenk C. S., Jenkins A., Lovell M. R., Helly J. C., Li B., Gao L., 2017, *MNRAS*, 464, 4520  
 Boyarsky A., Ruchayskiy O., Iakubovskiy D., Franse J., 2014, *Phys. Rev. Lett.*, 113, 251301  
 Bulbul E., Markevitch M., Foster A., Smith R. K., Loewenstein M., Randall S. W., 2014, *ApJ*, 789, 13  
 Chen J., Kravtsov A. V., Keeton C. R., 2003, *ApJ*, 592, 24  
 Diemand J., Kuhlen M., Madau P., Zemp M., Moore B., Potter D., Stadel J., 2008, *Nature*, 454, 735  
 Efstathiou G., 1992, *MNRAS*, 256, 43P  
 Gao L., Frenk C. S., Boylan-Kolchin M., Jenkins A., Springel V., White S. D. M., 2011, *MNRAS*, 410, 2309  
 Green A. M., Hofmann S., Schwarz D. J., 2005, *J. Cosmol. Astropart. Phys.*, 8, 003  
 Hellwing W. A., Frenk C. S., Cautun M., Bose S., Helly J., Jenkins A., Sawala T., Cytowski M., 2016, *MNRAS*, 457, 3492  
 Hezaveh Y. D. et al., 2016, *ApJ*, 823, 37  
 Kang X., Macciò A. V., Dutton A. A., 2013, *ApJ*, 767, 22  
 Kennedy R., Frenk C., Cole S., Benson A., 2014, *MNRAS*, 442, 2487  
 Koopmans L. V. E., 2005, *MNRAS*, 363, 1136  
 Li R., Frenk C. S., Cole S., Gao L., Bose S., Hellwing W. A., 2016, *MNRAS*, 460, 363  
 Lovell M. R. et al., 2012, *MNRAS*, 420, 2318  
 Lovell M. R., Frenk C. S., Eke V. R., Jenkins A., Gao L., Theuns T., 2014, *MNRAS*, 439, 300  
 Lovell M. R., Bertone G., Boyarsky A., Jenkins A., Ruchayskiy O., 2015, *MNRAS*, 451, 1573  
 Lovell M. R. et al., 2016, *MNRAS*, 461, 60  
 McKean J. et al., 2015, in *Proc. Sci., Advancing Astrophysics with the Square Kilometre Array (AASKA14)*. p. 84  
 Metcalf R. B., 2005, *ApJ*, 629, 673  
 Minor Q. E., Kaplinghat M., Li N., 2016, preprint ([arXiv:1612.05250](https://arxiv.org/abs/1612.05250))  
 Navarro J. F., Frenk C. S., White S. D. M., 1997, *ApJ*, 490, 493  
 Neto A. F. et al., 2007, *MNRAS*, 381, 1450  
 Sawala T., Pihajoki P., Johansson P. H., Frenk C. S., Navarro J. F., Oman K. A., White S. D. M., 2016a, *MNRAS*, preprint ([arXiv:1609.01718](https://arxiv.org/abs/1609.01718))  
 Sawala T. et al., 2016b, *MNRAS*, 456, 85  
 Schneider A., Smith R. E., Macciò A. V., Moore B., 2012, *MNRAS*, 424, 684  
 Sheth R. K., Tormen G., 1999, *MNRAS*, 308, 119  
 Skidmore W., TMT International Science Development Teams Science Advisory Committee TMT, 2015, *Res. Astron. Astrophys.*, 15, 1945  
 Springel V., Wang J., Vogelsberger M., Ludlow A., Jenkins A., Helmi A., Navarro J. F., Frenk C. S., 2008a, *MNRAS*, 391, 1685  
 Springel V. et al., 2008b, *Nature*, 456, 73  
 Vegetti S., Koopmans L. V. E., 2009a, *MNRAS*, 392, 945  
 Vegetti S., Koopmans L. V. E., 2009b, *MNRAS*, 400, 1583  
 Vegetti S., Lagattuta D. J., McKean J. P., Auger M. W., Fassnacht C. D., Koopmans L. V. E., 2012, *Nature*, 481, 341  
 Vegetti S., Koopmans L. V. E., Auger M. W., Treu T., Bolton A. S., 2014, *MNRAS*, 442, 2017  
 Wambsgans J., Bode P., Ostriker J. P., 2005, *ApJ*, 635, L1  
 Wang L. et al., 2016, *MNRAS*, preprint ([arXiv:1612.04540](https://arxiv.org/abs/1612.04540))  
 Xu D. D. et al., 2009, *MNRAS*, 398, 1235  
 Xu D., Sluse D., Gao L., Wang J., Frenk C., Mao S., Schneider P., Springel V., 2015, *MNRAS*, 447, 3189

This paper has been typeset from a  $\text{\TeX}/\text{\LaTeX}$  file prepared by the author.